

Free energy calculations along entropic pathways: II. Droplet nucleation in binary mixtures.

Caroline Desgranges and Jerome Delhommelle

Department of Chemistry, University of North Dakota, Grand Forks ND 58202

(Dated: August 25, 2021)

Abstract

Using molecular simulation, we study the nucleation of liquid droplets from binary mixtures and determine the free energy of nucleation along entropic pathways. To this aim, we develop the $\mu_1\mu_2VT - S$ method, based on the grand-canonical ensemble modeling the binary mixture, and use the entropy of the system S as the reaction coordinate to drive the formation of the liquid droplet. This approach builds on the advantages of the grand-canonical ensemble, which allows for the direct calculation of the entropy of the system and lets the composition of the system free to vary throughout the nucleation process. Starting from a metastable supersaturated vapor, we are able to form a liquid droplet by gradually decreasing the value of S , through a series of umbrella sampling simulations, until a liquid droplet of a critical size has formed. The $\mu_1\mu_2VT - S$ method also allows us to calculate the free energy barrier associated with the nucleation process, to shed light on the relation between supersaturation and free energy of nucleation, and to analyze the interplay between the size of the droplet and its composition during the nucleation process.

I. INTRODUCTION

The nucleation of liquid droplets is a ubiquitous phenomenon, central to many applications in chemistry, physics and atmospheric sciences^{1–49}. Nucleation from a single component system can be rationalized in terms of a change in a single intrinsic variable, such as e.g. the chemical potential or pressure. In this case, the supersaturation of the parent vapor phase is simply characterized by a given value of the pressure^{35,48–53} (or equivalently of the chemical potential) that departs from the pressure at coexistence. On the other hand, nucleation from a mixture involves a myriad of pathways arising from the larger dimension of the system, with as additional intrinsic variables, the mole fractions for each of the components^{54–70}. This also makes the definition of an appropriate reaction coordinate for the system especially challenging since, for instance, the total number of particles in the cluster is not the only significant variable, as the numbers of particles of each type also need to be taken into account to fully characterize the nucleation process. Here, we propose and implement a new approach that uses the entropy S , which captures the interplay between size increase and molecular selectivity during nucleation, as the reaction coordinate for the process.

The aim of this work is to shed light on the entropic pathways followed during the nucleation of two binary mixtures. The first example we consider is a binary mixture of two highly miscible gases, specifically the *Ar* – *Kr* mixture. The second example involves a mixture of carbon dioxide with an alkane (here, as an example we consider C_2H_6) that is of technological relevance for the oil industry and for separation applications. We develop here the $\mu_1\mu_2VT - S$ method, where μ_1 and μ_2 are the chemical potentials for the two components of the mixture and V and T are the volume and temperature of the system, to simulate the nucleation of a liquid droplet for these two binary mixtures. In the first paper of the series⁷¹, we discussed how, in the case of a single component system, the $\mu VT - S$ approach provided a direct connection with classical nucleation theory⁷², as any arbitrary value of μ (or, equivalently, of the supersaturation $\Delta\mu$) could be applied, and allowed the system to overcome the free energy barrier of nucleation. In practice, this was achieved by using the entropy of the system, which can be readily calculated in the grand-canonical ensemble, as the reaction coordinate and by driving the system along an entropic pathway using the umbrella sampling simulation technique. Extending this approach to the case of mixtures is especially appealing since the grand-canonical ensemble naturally allows the number of

molecules of each component to vary as nucleation proceeds. It is therefore very well suited to shed light on the impact of the choice of a given supersaturation (i.e. $\Delta\mu_1$ and $\Delta\mu_2$ for a binary mixture) on the free energy barrier of nucleation as well as on the interplay between the size of the droplet and its composition as nucleation takes place.

The paper is organized as follows. In the next section, we present the simulation method as well as the molecular models used in this work. We explain how we set up the $\mu_1\mu_2VT - S$ simulations, detailing how we proceed with the choice of chemical potentials, supersaturations, range of entropies to be sampled and the relation between the conditions of nucleation and the composition of the bulk. We then discuss the results obtained during the simulations of the nucleation process from supersaturated vapor phases of $Ar - Kr$ and $CO_2 - C_2H_6$. For all systems, we determine the free energy profile of nucleation and show how the choice of the conditions of nucleation impacts the height of the free energy barrier. We also focus on the analysis of the nucleation mechanism and on unraveling the interplay between size and composition during the formation of the liquid droplet, before finally drawing the main conclusions from this work in the last section.

II. SIMULATION METHOD

A. Spanning entropic pathways

We extend to the case of mixtures the simulation method developed in the first paper in this series⁷¹. The approach proposed is termed as $\mu VT - S$ and consists in sampling configurations of the system around a value of the entropy S_0 in the grand-canonical (μVT) ensemble. As discussed in the first part of this series, the $\mu VT - S$ simulation method provides a direct connexion with classical nucleation theory⁷², since simulations of the nucleation process can be carried out for any value of the supersaturation $\Delta\mu$. Another advantage of this method is that it allows the calculation of the entropy of the system S . In the case of binary mixtures, we therefore define the method as $\mu_1\mu_2VT - S$ and evaluate the entropy during the simulations through

$$S = \frac{U - N_1\mu_1 - N_2\mu_2}{T(N_1 + N_2)} \quad (1)$$

where μ_1 and μ_2 are the chemical potentials for the binary mixture, N_1 and N_2 are the

number of atoms/molecules for each of the two components and U is the internal energy for the entire system given by, in the case of a binary mixture of atoms,

$$U = U_{pot} + \frac{3}{2}N_1k_B T + \frac{3}{2}N_2k_B T \quad (2)$$

where U_{pot} is the potential energy for the system. In the case of linear molecules, we add a contribution of $k_B T$ per molecule to account for the rotational degrees of freedom.

The $\mu_1\mu_2VT - S$ simulation relies on gradually decreasing the entropy of the system through the application of a bias potential. This bias potential is defined within the framework of the umbrella sampling technique as

$$U_{bias} = \frac{1}{2}k(S - S_0)^2 \quad (3)$$

in which S_0 is the target value for the entropy, S is the current value of the entropy of the system and k is a spring constant. This bias potential is then added to the potential energy of the system, and the total potential energy is used in the conventional Metropolis criteria for the acceptance of the different types of Monte-Carlo (MC) steps. For the $Ar - Kr$ mixture, MC steps include the insertion (12.5 % of the attempted MC steps) or deletion (12.5 % of the attempted MC steps) of atoms as well as the translation of a single atom (75 % of the attempted MC steps). In the case of the $C_2H_6 - CO_2$ mixture, we have the following rates: rotation (37.5 % of the attempted MC steps), translation (37.5 %), insertion (12.5 %) and deletion (12.5 %).

Successive umbrella simulations with decreasing values for the target entropy (S_0) are carried out to achieve the formation of a liquid droplet of a critical size. During each of these simulations, histograms for the number of times a given entropy interval is visited are collected, allowing for the calculation of the free energy profile associated with the nucleation process^{70,73-76}.

B. Simulation models

The simulation models used in this work for Ar and Kr are based on the Lennard-Jones potential⁷⁷, with the following parameters for Ar : $\sigma_{Ar}=3.3952 \text{ \AA}$ and $\epsilon_{Ar}/k_B=116.79 \text{ K}$ and for Kr : $\sigma_{Kr}=3.6274 \text{ \AA}$ and $\epsilon_{Kr}/k_B=162.58 \text{ K}$.

For the $CO_2 - C_2H_6$, we use a force field that models the dispersion-repulsion interactions through an exp-6 functional form^{78–81}.

$$\begin{aligned}
 u(r) &= \frac{\epsilon}{1-6/\alpha} \left[\frac{6}{\alpha} \exp \left(\alpha \left[1 - \frac{r}{r_m} \right] \right) - \left(\frac{r_m}{r} \right)^6 \right] & (r > r_{max}) \\
 &= \infty & (r < r_{max})
 \end{aligned}
 \tag{4}$$

In Eq. 4, r_m is the distance for which the potential reaches a minimum, r_{max} is the smallest positive distance for which $du(r)/dr = 0$ and ϵ and α are two potential parameters. As discussed by Errington *et al.*⁷⁹, it is convenient to discuss the potential parameters in terms of σ (i.e. the distance for which $u(r) = 0$, obtained numerically by solving the equation $u(\sigma) = 0$) rather than in terms of r_m . In the case of C_2H_6 , we use an united atom-type force field and model the molecule with two exp-6 sites, each site standing for a CH_3 group. We use the following set of parameters: $\epsilon_{CH_3}/k_B = 129.64$ K, $\sigma_{CH_3} = 3.679$ Å and $\alpha_{CH_3} = 16$. In the case of CO_2 , in addition to the the repulsion-dispersion interactions, a Coloumbic term is added to account for the quadrupolar nature of CO_2 . The CO_2 molecule is modeled with a distribution of three exp-6 sites and three point charges located on each of the atoms. We use the following parameters for the exp-6 sites: $\epsilon_C/k_B = 29.07$ K, $\sigma_C = 2.753$ Å and $\alpha_C = 14$, $\epsilon_O/k_B = 83.20$ K, $\sigma_O = 3.029$ Å and $\alpha_O = 14$. We also have $q_C = 0.6466$ e and $q_O = -0.3233$ e. Both molecules are considered to be rigid, with a distance between the two CH_3 exp-6 sites set to 1.839 Å for ethane and a length of the $C - O$ bond fixed to 1.1433 Å for CO_2 . The calculation of the interaction energy is performed for distances up to 13.5 Å for both systems with, electrostatic interactions calculated with the Ewald sum method beyond that distance using the parameters given in previous work⁸². In line with previous simulation work on nucleation³⁵, we do not include any tail corrections for the dispersion-repulsion interactions beyond the cutoff distance.

C. Setting up the simulation

1. Ar - Kr mixture

We carry out $\mu_1\mu_2VT - S$ simulations for the $Ar - Kr$ mixture at $T = 148.15$ K in cubic cells with an edge of 100 Å (the usual periodic boundary conditions are applied). We take advantage of the Expanded Wang-Landau (EWL) method we recently developed^{82–85}

to obtain very accurate estimates for μ_1 and μ_2 both at the vapor-liquid coexistence and for supersaturated vapor phases, which will be the parent phase for the nucleation events. The values are presented in Table I

TABLE I: *Ar* – *Kr* mixture at 148.15 K: chemical potentials for *Ar* (μ_1) and *Kr* (μ_2), supersaturations, mole fractions in *Kr* for the vapor (y_{Kr}) and for the liquid (x_{Kr}), pressure and entropies for the two coexistence points (coex I and coex II) and for the supersaturated vapors considered in this work (system 1 to 4).

	μ_1 (kJ/mol)	μ_2 (kJ/mol)	$\Delta\mu_1$ (kJ/mol)	$\Delta\mu_2$ (kJ/mol)	x_{Kr}	y_{Kr}	P bar	P/P_{coex}	S_l (kJ/mol/K)	S_v (kJ/mol/K)
coex I	-14.077	-17.571	-	-	0.440	0.190	28.68	1.0	0.0848	0.1074
system 1	-13.951	-17.463	0.049	0.108	0.440	-	57.27	2.0	0.0831	-
system 2	-13.930	-17.439	0.070	0.132	0.440	-	63.09	2.2	0.0828	-
coex II	-13.720	-18.165	-	-	0.250	0.108	36.92	1.0	0.0845	0.1021
system 3	-13.548	-18.057	0.172	0.108	0.250	-	73.83	2.0	0.0817	-
system 4	-13.514	-18.039	0.206	0.126	0.250	-	81.28	2.2	0.0813	-

We start by determining the conditions for the vapor-liquid coexistence at the coex I point. In practice, this is done using the EWL method by finding numerically the values for μ_1 and μ_2 which lead to equal probabilities for the vapor and the liquid phase (see more details in previous work⁸²). The EWL method also allows to obtain all thermodynamic properties for the mixture including the mole fractions, pressure as well as the entropies for the two coexisting phases. These entropies, which are also given in Table I, provide an idea of the range of entropies that need to be sampled for the system to undergo the vapor \rightarrow liquid transition. From the coexistence point, we can increase the value of the two chemical potentials μ_1 and μ_2 or, in other words, create a supersaturated vapor that will serve as a starting point for the nucleation process. We list in Table I the two sets of supersaturations (system 1 and system 2) generated from the coexistence point coex I. As can be seen from Table I, increasing $\Delta\mu$ brings the supersaturated vapor more deeply into the liquid domain of the phase diagram, resulting in a larger value for the pressure and a lower value for the entropy of the liquid. We proceed along the same lines from the second coexistence point (coex II) to define two supersaturated vapors (system 3 and system 4), this time with a

mole fraction in the liquid (x_{Kr} set to 0.250). We finally add that there are other ways of determining the chemical potential at the vapor-liquid coexistence and for supersaturated vapors^{78,86-97}.

We plot in Fig. 1 the successive umbrella sampling windows carried out during the $\mu_1\mu_2VT - S$ simulations on system 1. Fig. 1 shows the histograms corresponding to the probability according to which a given entropy interval is visited during the $\mu_1\mu_2VT - S$ simulations. Each of the umbrella sampling windows (labeled with an index i) is obtained by imposing through Eq 3 a different value of the target entropy $S_{0,i}$. During the nucleation of a liquid droplet, the system goes from a supersaturated vapor with a low density, and thus of high entropy, to a system containing a liquid droplet of a critical size, i.e. to a much more dense system of lower entropy. To observe the formation of the liquid droplet, we therefore carry out successive umbrella sampling windows for decreasing values of the target entropy $S_{0,i}$ and obtain the histograms, shown in Fig. 1, that cover the entire nucleation process. The progress of the system towards the formation of a liquid droplet can be followed by monitoring the relative location of $S_{max,i}$, the entropy for which the histogram $p_i(S)$ reaches its maximum, and of $S_{0,i}$, the target entropy for the i^{th} umbrella sampling window. We start with the window located to the right of Fig. 1, associated with the largest value of $S_{0,1}$ which corresponds to a very dilute vapor ($S_{0,1} = 0.11$ kJ/mol/K). As shown in Fig. 1, for the first window (starting from the right), we have $S_{max,1} = 0.1097$ kJ/kg/K, which is less than the target value $S_{0,1} = 0.11$ kJ/kg/K. This means that the target value $S_{0,1}$ is greater than the entropy of the metastable supersaturated vapor for the choice of (μ_1, μ_2) made for system 1. Gradually decreasing the target entropy for the next windows allows us to find the value $S_{0,i}$ which coincides with the maximum for $p_i(S)$. This occurs here for $S_{max,i} = S_{0,i} = 0.1091$ kJ/kg/K. At this point, we have the metastable supersaturated vapor. Then, during the next few umbrella sampling windows, we observe a change in behavior as the histograms $p_i(S)$ now lag behind the target value for the entropy with $S_{max,i} > S_{0,i}$. This corresponds to the fact that the system has to overcome the free energy cost in forming the liquid droplet. Later on, for $S_{0,i} = 0.103$ kJ/kg/K, we find again that the maximum for $p_i(S)$ coincides with $S_{0,i}$, indicating that we have reached the top of the free energy barrier of nucleation and that a liquid droplet of a critical size has formed. For target values of the entropy greater than 0.103 kJ/kg/K, we observe again a change in behavior as the histograms $p_i(S)$ run ahead of the target value for the entropy with $S_{max,i} < S_{0,i}$,

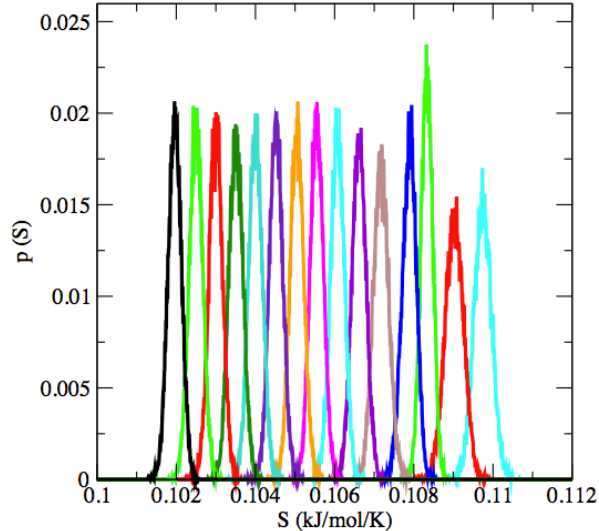


FIG. 1: *Ar* – *Kr* mixture (system 1). Histograms $p(S)$ collected during the umbrella sampling simulations for decreasing values for the entropy.

corresponding to the spontaneous growth of the liquid droplet.

To provide additional insight in the evolution of the average properties of the system for different umbrella sampling windows, we show in Fig 2 the potential energy and the number of atoms for different values of the target entropy $S_{0,i} = 0.107$ kJ/mol/K and $S_{0,i} = 0.104$ kJ/mol/K during a production run. These plots show the impact of decreasing the target value for the entropy on the system. For example, comparing the results for two different umbrella sampling windows, 0.107 kJ/mol/K and 0.104 kJ/mol/K, we observe a decrease in the potential energy by about 60 %. This happens simultaneously with an increase in the number of atoms of each component in the mixture by about 15 % for *Ar* and by 20 % for *Kr*. This confirms that the decrease in the target value for the entropy occurs with a greater organization and density of the system, that we will analyze in depth in the 'Results' section. We finally add that, for each umbrella sampling window, we run an equilibration run of 100×10^6 MC steps, followed by a production run of 200×10^6 MC steps. Throughout the $\mu_1\mu_2VT - S$ simulations, we also check that the acceptance rate for the insertion/deletion steps remains high enough to ensure an accurate sampling of the configurations of the systems. For instance, in the case of system 1 and for the configurations of highest density (umbrella sampling window with a critical liquid droplet for $S_{0,i} = 0.103$ kJ/mol/K), the acceptance rates for the insertion/deletion steps are of

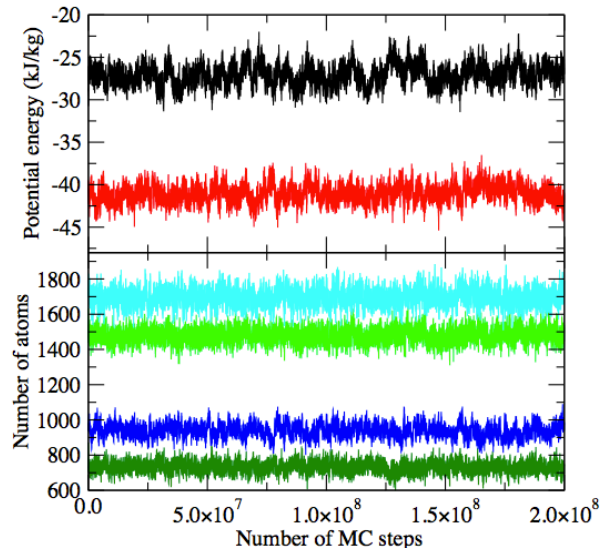


FIG. 2: $Ar - Kr$ mixture for a supersaturation of 2 at $x_{Ar} = 0.56$ and at $T = 148.15$ K. (Top) Potential energy of the system during a simulation at entropy fixed to $S_0 = 0.107$ kJ/mol/K (black) and $S_0 = 0.104$ kJ/mol/K (red). (Bottom) Number of atoms during the simulation at $S_0 = 0.107$ kJ/mol/K (N_{Ar} : light green and N_{Kr} : dark green) and at $S_0 = 0.104$ kJ/mol/K (N_{Ar} : cyan and N_{Kr} : blue).

45.8 %.

2. $C_2H_6 - CO_2$ mixture

Simulations of droplet nucleation for the $C_2H_6 - CO_2$ mixture are performed at $T = 263.15$ K in cubic cells, with an edge of 100 \AA , and with the usual periodic boundary conditions. We use EWL simulations to determine the other input parameters for the $\mu_1\mu_2VT - S$ simulations and list in Table II the sets of chemical potentials (μ_1, μ_2) used for these simulations.

We identify a first state point, coex III, leading to vapor-liquid coexistence for the $C_2H_6 - CO_2$ mixture. As previously discussed, this is achieved by finding numerically μ_1 and μ_2 such that the liquid and the vapor phases are equally probable. The EWL simulations also yield the mole fractions as well as the entropies of the two coexisting phases, bracketing the range of entropies needed to sample the nucleation of the liquid droplet. From coex

TABLE II: $C_2H_6 - CO_2$ mixture at 263.15 K: chemical potentials for C_2H_6 (μ_1) and CO_2 (μ_2), supersaturations, mole fractions in CO_2 for the vapor (y_{CO_2}) and for the liquid (x_{CO_2}), pressure and entropies for the two coexistence points (Coex III and Coex IV) and for the supersaturated vapors considered in this work (system 5 to 8).

	μ_1 (kJ/mol)	μ_2 (kJ/mol)	$\Delta\mu_1$ (kJ/mol)	$\Delta\mu_2$ (kJ/mol)	x_{CO_2}	y_{CO_2}	P bar	P/P_{coex}	S_l (kJ/mol/K)	S_v (kJ/mol/K)
coex III	-38.186	-44.397	-	-	0.053	0.124	27.37	1.0	0.1397	0.1556
system 5	-38.055	-44.268	0.131	0.129	0.053	-	43.80	1.6	0.1318	-
system 6	-38.036	-44.250	0.150	0.147	0.053	-	46.53	1.7	0.1316	-
coex IV	-38.261	-43.216	-	-	0.097	0.201	29.60	1.0	0.1409	0.1566
system 7	-38.121	-43.076	0.140	0.140	0.097	-	47.35	1.6	0.1333	-
system 8	-38.099	-43.061	0.162	0.155	0.097	-	50.32	1.7	0.1331	-

III, we increase the chemical potentials of the two mixture components by $\Delta\mu_1$ and $\Delta\mu_2$ to obtain thermodynamic conditions located in the domain of the liquid in the phase diagram and, for which, we can observe a supersaturated vapor. We repeat this step for two different supersaturations leading to system 5 and 6 in Table II (as for $Ar - Kr$, the choices for $\Delta\mu_1$ and $\Delta\mu_2$ are made such that the liquid mole fraction in the second component, here CO_2 , remains constant). We choose another coexistence point, coex IV, and two corresponding supersaturated vapors, system 7 and system 8. For each umbrella sampling window, an equilibration run of 50×10^6 MC steps is run, followed by a production run of 100×10^6 MC steps. As with the $Ar - Kr$ mixture, we check that the acceptance rates for the insertion/deletion steps remains high enough to ensure an accurate sampling. This is the case here for all umbrella sampling windows. For instance, in the case of system 5 and for the window associated with the highest density (umbrella sampling window with a critical liquid droplet for $S_{0,i} = 0.155$ kJ/mol/K), the acceptance rates for the insertion/deletion steps are of 36.9 % for C_2H_6 and of 46.6 % for CO_2 .

III. RESULTS AND DISCUSSION

A. *Ar* – *Kr* mixture

We start by analyzing the free energy barriers obtained for the *Ar* – *Kr* mixture at $T = 148.15$ K. The left panel of Fig. 3 shows the free energy profiles for two different supersaturations, system 1 and system 2, at $x_{Kr} = 0.44$. The supersaturation has a direct effect on the height of the free energy barrier, with a barrier of $25 \pm 2 k_B T$ for system 1 and of $15 \pm 2 k_B T$ for a system 2. $\Delta\mu_1$ and $\Delta\mu_2$ are greater for system 2, which means that the parent supersaturated vapor of system 2 is located more deeply into the domain of the liquid in the phase diagram, and, as such, that the nucleation of a liquid droplet occurs more easily. This also leads to a lower free energy of nucleation than for system 1. We find that the range of entropies spanned during the nucleation process is also impacted by the amount of supersaturation. For instance, looking at system 2 in Fig. 3, we find that, for the higher supersaturation, the passage from the supersaturated vapor to a system containing a droplet of a critical size occurs over entropies between 0.1085 kJ/mol/K, for which the free energy reaches a minimum for the entropy of the metastable parent phase, and 0.1055 kJ/mol/K, for which the free energy reaches a maximum corresponding to the formation of a droplet of a critical size. On the other hand, for system 1 (lower supersaturation), we find that liquid nucleation takes place over a much broader entropy range, with the entropic pathway ranging from 0.1091 kJ/mol/K to 0.103 kJ/mol/K. This can be attributed to the combination of two effects. For a higher supersaturation, the density for the parent supersaturated vapor is larger and, therefore, its entropy is lower. Furthermore, at high supersaturation, the thermodynamic conditions lie further inside the liquid domain. Thus, the critical size for the liquid droplet becomes smaller, resulting in a system at the top of the free energy barrier that has a higher entropy. Both effects account for the narrowing, at high supersaturation, of the entropy range spanned during the droplet nucleation along the entropic pathway.

We now turn to the second set of simulations carried out for system 3 and system 4 at $x_{Kr} = 0.25$. The free energy profiles obtained for the two supersaturations are shown in the right panel of Fig. 3. The behavior observed for $x_{Kr} = 0.25$ exhibits similar qualitative features as for $x_{Kr} = 0.44$. We find that the height of the free energy barrier of nucleation increases as we go from system 4 to system 3 (as the supersaturation decreases), with the free

energy of nucleation increasing from $7 \pm 1 k_B T$ to $21 \pm 2 k_B T$. The range of entropies spanned during nucleation is also found to increase as the supersaturation decreases. For system 4, we observe that the entropy of the parent phase is of 0.1047 kJ/mol/K while the entropy at the top of the free energy barrier is of 0.103 kJ/mol/K. For a lower supersaturation (system 3), the entropy of the supersaturated vapor is 0.1055 kJ/mol/K while it is of 0.100 kJ/mol/K at the top of the free energy barrier. This means that a significantly broader range of entropies is sampled during the nucleation process. There are, however, notable differences between the two plots, which result from the interplay between pressure and the chemical composition of the system. Considering the results at fixed supersaturation, we find that the free energy of nucleation decreases by 16 % (going from system 1 to system 3), while it decreases by 53 % between system 2 and system 4. Similarly, the dependence of the height of the free energy barrier upon supersaturation is also shown to be impacted, with a decrease by 40 % from system 1 to system 2 at $x_{Ar} = 0.56$ and a much larger decrease by 66 % from system 3 to system 4 at $x_{Ar} = 0.75$. Both findings can be attributed to the fact that liquid mixtures with a lower fraction of Kr are obtained for higher pressures. This, in turn, implies that the corresponding parent phases will be supersaturated vapors of larger densities and, therefore, result in lower free energy barriers of nucleation.

The plot shown in Fig. 3 for the free energy profile of nucleation is a projection of the multi-dimensional free energy surface, as discussed in prior work on the nucleation in binary systems⁹⁸. Here, we do not take into account any nonisothermal effect during nucleation^{99,100}. To interpret further the results obtained for the free energy of nucleation as a function of S , we now focus on the interdependence between the entropy S , the droplet size and its composition. As we have seen from Fig. 2, the number of atoms steadily increases as the target entropy $S_{0,i}$ is decreased. To check that the decrease in entropy undergone by the system leads to an increased organization within the system and to the formation of a liquid droplet, we show in Fig. 4 snapshots of the system, obtained during umbrella sampling simulations for decreasing values for the target entropy. As $S_{0,i}$ decreases, the droplet size increases, with a larger number of atoms being incorporated to the droplet as the target entropy decreases from 0.1075 kJ/mol/K, to 0.105 kJ/mol/K, and finally to 0.103 kJ/mol/K. To assess further this point, we perform a detailed analysis of the size and composition of the droplet along the entropic pathway. The atoms belonging to the incipient droplet are identified through a commonly used geometric criterion³⁵. For this purpose, we determine

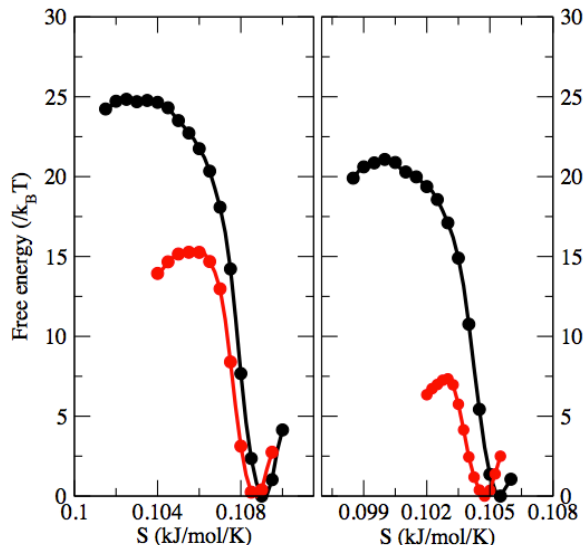


FIG. 3: Free energy barriers of nucleation for the $Ar - Kr$ mixture at $T = 148.15$ K. (Left panel) system 1 (black) and system 2 (red) for $x_{Ar} = 0.56$. (Right panel) system 3 (black) and system 4 (red) for $x_{Ar} = 0.75$

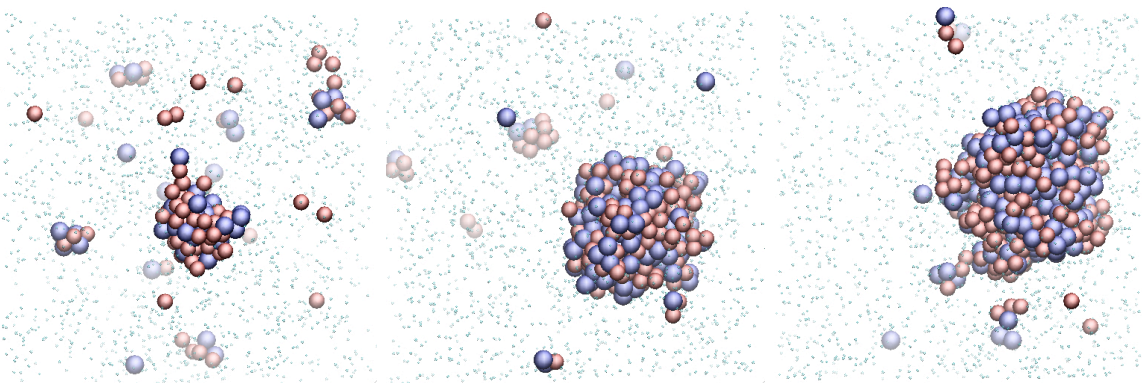


FIG. 4: $Ar - Kr$ mixture: Snapshots of system 1 during the nucleation process for a target entropy of 0.1075 kJ/mol/K (left), 0.105 kJ/mol/K (middle) and 0.103 kJ/mol/K (right). Atoms with a liquid-like environment are shown with larger spheres, with Ar in red and Kr in blue.

the distribution for the number of neighbors within a distance of 5.4 \AA of a central atom in the vapor and the liquid mixture. We show in Fig. 5 these distributions. Both distributions are sharply peaked around $N_{nab} = 1$ for the vapor and around $N_{nab} = 10$ for the liquid. As shown in Fig. 5, atoms belonging to the vapor always have less than 6 neighbors within a distance of 5.4 \AA . This allows us to introduce the following condition to identify a liquid-like

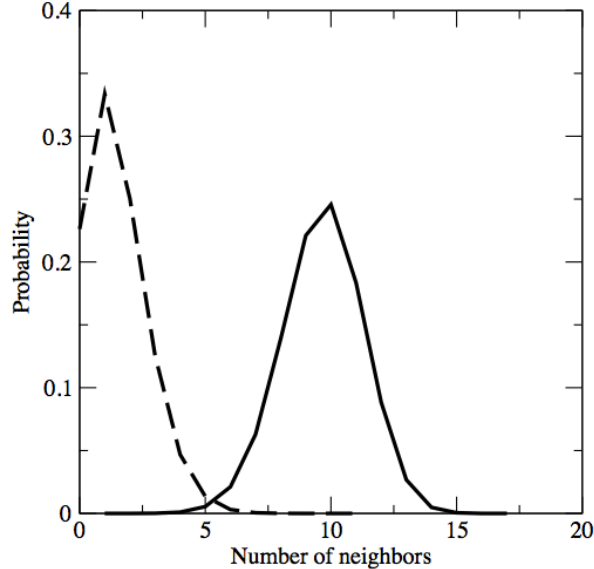


FIG. 5: $Ar - Kr$ mixture: Distributions for the number of neighbors within a distance of 5.4 \AA for the liquid (solid line) and for the vapor (dashed line) at coexistence for $T = 148.15 \text{ K}$.

atom, or equivalently an atom belonging to the developing droplet, as an atom with at least 6 nearest neighbors within 5.4 \AA .

Applying this analysis to the configurations generated during the umbrella sampling windows, leads to the determination of the evolution of the size of the droplet during the nucleation process. Furthermore, by keeping track of the identity (either Ar or Kr) of the atoms belonging to the droplet, we can also shed light on the chemical selectivity during the formation of the cluster. This means that the interplay between droplet size and composition during the nucleation process can be directly accessed during the simulations, and, in turn, shed light on the departure in composition of the critical droplet from the bulk composition^{55,64} and the possible onset of phase separation in partially miscible mixtures^{57,59,60}.

We show on the left of Fig. 6, the results obtained for the two supersaturations of systems 1 and 2. In both cases, throughout the nucleation process, the overall size of the droplet is shown to gradually increase as the entropy of the system decreases. The critical size of the droplet is found to be larger at low supersaturation ($N_c = 713 \pm 60$ for system 1 and $N_c = 323 \pm 30$ for system 2). It is also reached for a lower value of the entropy at low supersaturation ($S_c = 0.103 \text{ kJ/mol/K}$ for system 1) than at high supersaturation ($S_c = 0.1055 \text{ kJ/mol/K}$ for system 2), in line with the results obtained for the free energy barrier

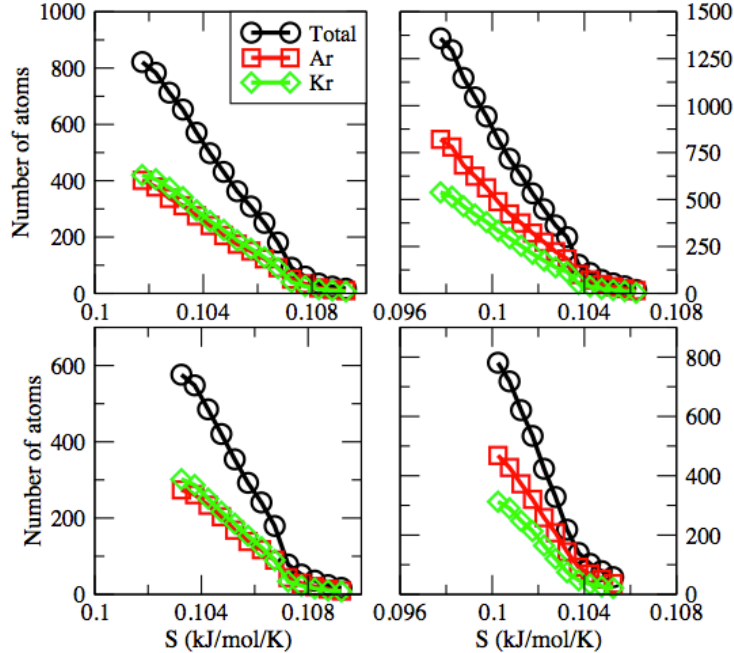


FIG. 6: $Ar - Kr$ mixture. (Left panel) Variation of the total number of atoms in the cluster and of the number of atoms for Ar and Kr at $x_{Ar} = 0.56$ for system 1 (top) and system 2 (bottom). (Right panel) Total number of atoms in the cluster, number of atoms for Ar and Kr against S at $x_{Ar} = 0.75$ for system 3 (top) and system 4 (bottom).

in Fig. 3. A closer inspection of the variation for the number of each type of atoms show that the composition of the droplet does not remain the same during the entire nucleation process. For small sizes (high entropy), the droplet is richer in Ar with 55 ± 5 % of Ar atoms in the droplet at $S = 0.1073$ kJ/mol/K for system 1. There is then a crossover at $S = 0.1067$ kJ/mol/K for which the two types of atoms are equally present. As the entropy further decreases, the droplet becomes richer in Kr atoms (with a fraction of 48 ± 4 % in Ar for a droplet of a critical size). Looking at the composition of the droplet past the critical size, we find that the fraction of Ar atoms in the droplet increases again and reaches 49 ± 4 % for $S = 0.102$ kJ/mol/K. The same mechanism is observed for system 2, with a crossover point located at $S = 0.1068$ kJ/mol/K and a fraction of Ar atoms of 47 ± 4 % in the critical droplet. These fluctuations in the nucleus composition through the nucleation process, as well as the departure of the composition of the droplet from the composition of the liquid phase, are consistent with prior work on nucleation, based on a revision of

the classical nucleation theory¹⁰¹, on classical density functional theory calculations⁵⁵, on molecular simulations^{60,62,64}, or on approaches based on macroscopic kinetics⁶⁸. Our results indicate that the mole fraction in *Ar* in the nucleus to be less than for the bulk by 0.08 for System 1 and of 0.03 for System 2 with respect to the bulk composition. These deviations, which are moderate due the almost ideal nature of the *Ar*–*Kr* mixture as noted by Zeng and Oxtoby⁵⁵, did not give rise to a significant phase separation effect as reported in simulations of more strongly asymmetric mixtures^{60,102}.

Looking now at the evolution of the size of the droplet as a function of entropy for the other set of conditions ($x_{Ar} = 0.75$), we see that the size of the droplet steadily increases as the entropy of the system decreases. The droplet reaches a size of 629 ± 90 atoms for the critical droplet in the case of system 3, and a size of 273 ± 50 for system 4. As for the previous system, the critical droplet has formed once the entropy has reached a critical value $S_c = 0.100$ kJ/mol/K for system 3, a value that is notably lower than its counterpart of 0.103 for system 4. This reflects the fact that the range for the entropies spanned during the nucleation event becomes narrower and narrower as the supersaturation is increased. Unlike for systems 1 and 2, we do not observe any crossover between the mole fractions in *Ar* and *Kr* in the droplet, given the very large fraction of *Ar* in systems 3 and 4. As for systems 1 and 2, we observe, however, fluctuations in the composition of the droplet with the fraction of *Ar* atoms in the droplet varying between 60 % and 80 % during nucleation.

B. $CO_2 - C_2H_6$ mixture

Turning to the results obtained for the $CO_2 - C_2H_6$ mixture, we plot in Fig. 7, the free energy barrier of nucleation obtained for systems 5 and 6. For a liquid fraction of $x_{CO_2} = 0.053$ (left panel of Fig. 7), we observe that increasing the supersaturation leads to a decrease in the height of the free energy barrier of nucleation from $21 \pm 2 k_B T$ (system 5) to $12 \pm 1 k_B T$ (system 6). Similarly, for a mole fraction of $x_{CO_2} = 0.097$, a lower supersaturation results in a barrier of $12 \pm 1 k_B T$ (system 7), while a higher supersaturation yields a free energy of nucleation of $7 \pm 1 k_B T$ (system 8). The range of entropies spanned along the nucleation pathway is also found to depend strongly on supersaturation, and becomes broader at lower supersaturations. For instance, for system 5, we obtain an entropy for the parent (supersaturated vapor) phase of 0.161 kJ/mol/K and an entropy of the system

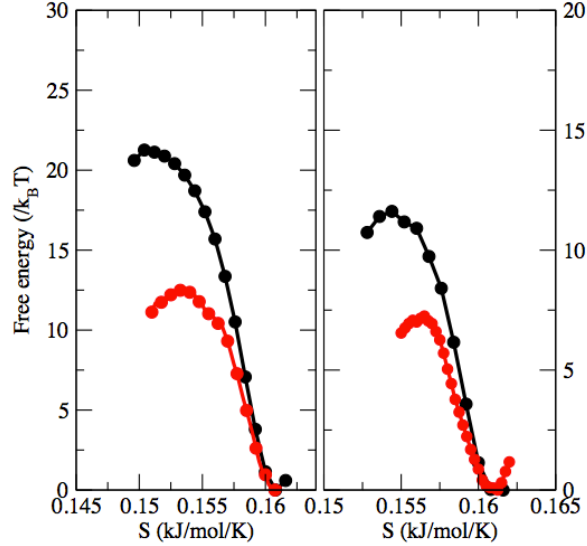


FIG. 7: Free energy barriers of nucleation for the $CO_2 - C_2H_6$ mixture at $T = 263.15$ K. (Left panel) System 5 (black) and system 6 (red) for $x_{CO_2} = 0.053$. (Right panel) System 7 (black) and system 8 (red) for $x_{CO_2} = 0.097$

of $S_c = 0.151$ kJ/mol/K, when a droplet of a critical size has formed. Increasing the supersaturation (system 6) leads to a narrower entropy range, most notably as a result of a decrease in the entropy $S_c = 0.154$ kJ/mol/K for which the critical size of the droplet is reached. Similar conclusions apply for systems 7 and 8. We find a narrowing of the entropy range spanned during nucleation at high supersaturation, with the top of the free energy barrier droplet reached for a higher entropy ($S_c = 0.157$ kJ/mol/K) than at low supersaturation ($S_c = 0.155$ kJ/mol/K). The higher entropy required to form a droplet of a critical size at high supersaturation, together with the lower free energy barrier of nucleation obtained at high supersaturation, are most likely due to the smaller size of the critical droplet at high supersaturation, a point that we discuss in the next section in our analysis of the relation between size, selectivity and entropy during the nucleation process.

We show in Fig. 8 snapshots of configurations of system 5, obtained throughout the nucleation process. As for the $Ar - Kr$ system, we start from a metastable supersaturated vapor and carry out umbrella sampling windows with decreasing values for the target entropy. During the first few umbrella sampling windows, the target entropy is high enough, so that the droplet is fairly small (see on the left of Fig. 8 for $S_{0,i} = 0.157$ kJ/kg/K). Then, as $S_{0,i}$

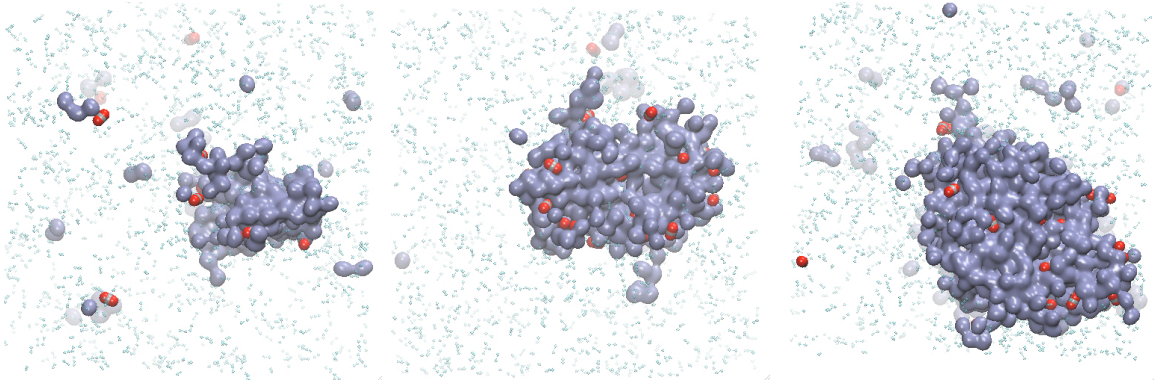


FIG. 8: $C_2H_6 - CO_2$ mixture: Snapshots of system 5 during the nucleation process for a target entropy of 0.157 kJ/mol/K (left), 0.154 kJ/mol/K (middle) and 0.151 kJ/mol/K (right). Molecules with a liquid-like environment are shown with larger spheres, with the CO_2 molecules identified through their O atoms shown in red.

is decreased further, the droplet starts to become larger and larger, and eventually reaches its critical size for $S_{0,i} = 0.151$ kJ/kg/K. This shows that decreasing the value for the target entropy not only increases the density of the system, but also results in an increased level of organization with the formation of the liquid droplet.

As for the Ar-Kr mixture, Fig. 7 shows a projection of the multi-dimensional free energy surface in the (entropy, free energy) plane. We pursue our analysis by characterizing the interdependence between the entropy S , the droplet size and its composition. We start by determining which molecules in the system have a liquid-like environment and, as such, belong to the droplet. We determine, for each molecule, the distributions, shown in Fig. 9, for the number of neighbors for the vapor and the liquid. Neighboring molecules are defined as being separated by a distance (between the centers of mass of the 2 neighboring molecules) less than 6.4 \AA . The distributions obtained for the vapor and liquid reach their maxima for very different numbers of neighbors (for, on average, a single neighbor in the case of the vapor and for 9 neighbors in the case of the liquid). This allows us to define a molecule as having a liquid-like environment. and thus belonging to the droplet, if it has 6 or more neighbors within a spherical shell of 6.4 \AA .

We now move on to the analysis of the size of the droplet as a function of the entropy of the system throughout the nucleation process. Fig. 10 shows that, for all systems, the total number of molecules within the cluster increases smoothly as the entropy of the system

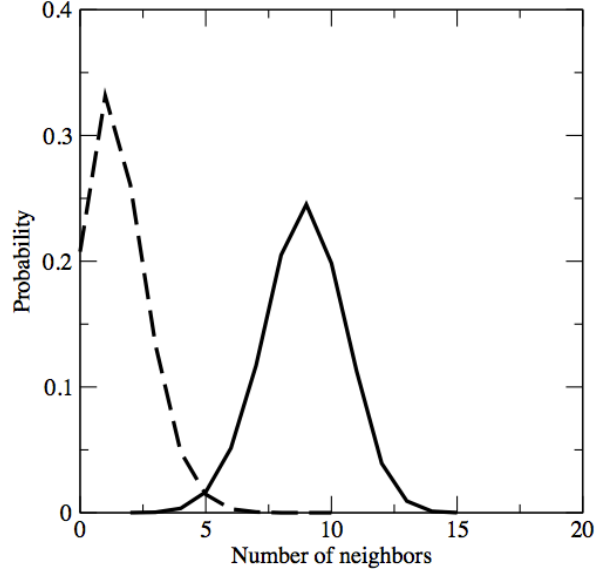


FIG. 9: $CO_2 - C_2H_6$ mixture: Distributions for the number of neighbors within a distance of 6.4 \AA for the liquid (solid line) and for the vapor (dashed line) at coexistence for $T = 263.15 \text{ K}$.

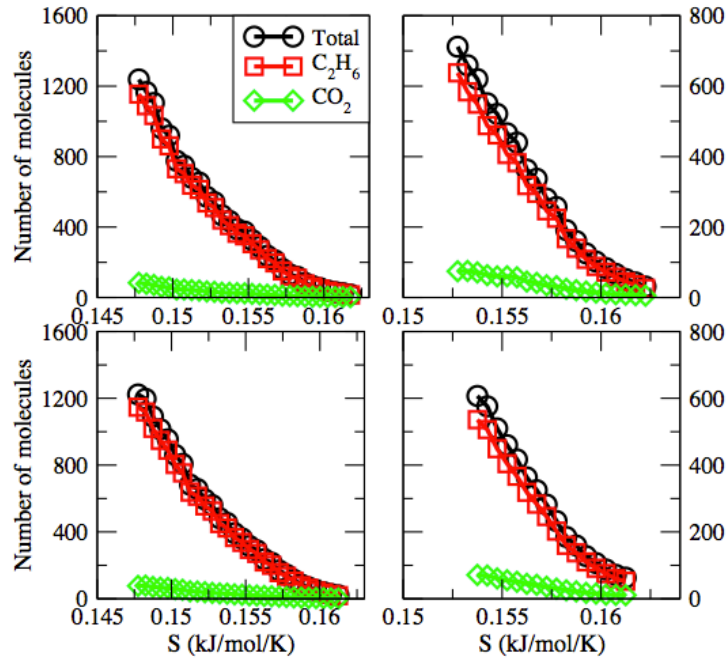


FIG. 10: $C_2H_6 - CO_2$ mixture. (Left panel) Variation of the total number of molecules in the cluster and of the number of molecules for C_2H_6 and CO_2 at $x_{CO_2} = 0.053$ for system 5 (top) and system 6 (bottom). (Right panel) Total number of molecules in the cluster, number of molecules for C_2H_6 and CO_2 against S at $x_{CO_2} = 0.097$ for system 7 (top) and system 8 (bottom).

decreases. Furthermore, we find that the size of the critical droplet decreases as supersaturation is increased. For a liquid mole fraction of $x_{CO_2} = 0.053$, the critical size for the droplet is of $N_c = 715 \pm 35$ molecules for system 5 and of $N_c = 422 \pm 30$ molecules for system 6. The smaller size of the critical droplet at high supersaturation (system 6) accounts for the higher value of the entropy for which the system reaches the top of the free energy barrier. Similarly, when the liquid mole fraction $x_{CO_2} = 0.097$, the critical size is of $N_c = 494 \pm 28$ molecules for a low supersaturation (system 7) and of $N_c = 303 \pm 21$ molecules for a high supersaturation (system 8). The smaller critical size and higher critical entropy obtained at the higher supersaturation are, once again, found to be consistent with the free energy plot of Fig. 7. Turning to the composition of the droplet, we find that C_2H_6 remains predominant throughout the nucleation process for all systems (see Fig. 10). We also find, however, that the composition of the nucleus depends on its size, as nucleation starts with the formation of a droplet that has a higher CO_2 mole fraction than the bulk. It is around 8 % for systems 5 and 6 for droplets containing a total of 50 – 100 molecules. Similarly, considering the same droplet sizes, it is of about 17 % for systems 7 and 8. The fraction of CO_2 then decreases as the size of the droplet increases. For droplets of a critical size, the fraction of CO_2 is of 6 % for systems 5 and 6, while it is of 13 % for systems 7 and 8. Despite the small sizes of the critical droplets, which contain only a few hundred of molecules, the fractions in the critical droplets are reasonably close to the CO_2 mole fraction of the liquid, and the departure from the bulk compositions (5.3 % of CO_2 for systems 5 and 6, and 9.7 % of CO_2 for systems 7 and 8) is small. As for binary mixtures of atoms, the departures in the droplet composition with respect to that of the bulk are consistent with prior simulations of droplet nucleation in binary molecular systems (see e.g. recent simulations of the methane-nonane system⁶⁴).

IV. CONCLUSION

In this work, we propose a new simulation method to study the nucleation process in binary mixtures of atomic fluids ($Ar - Kr$) and of molecular fluids ($C_2H_6 - CO_2$). The method is based on driving the formation of a liquid droplet through a series of umbrella sampling simulations where the bias potential is a function of the entropy S of the system. The resulting approach is implemented within the grand-canonical ensemble and, since the entropy serves as the reaction coordinate for the nucleation process, is called $\mu_1\mu_2VT - S$.

The application of the method to the formation of liquid droplets in binary mixtures sheds light on the interplay between the size of the droplet, its composition and the supersaturation at which the nucleation process occurs. Our findings show that, at low supersaturation, the range of entropies spanned by the nucleation process becomes broader, as a result of the combined effect of the larger entropy of the metastable supersaturated vapor (parent phase) and of the lower entropy associated with the configurations of the system that contain a liquid droplet of a critical size. These simulations allow us to characterize the critical droplet in terms of a critical value reached by the entropy at the top of the free energy barrier of nucleation. We are also able to obtain the free energy profile along the entropic pathway underlying the formation of the liquid droplet and to calculate the free energy of nucleation as a function of the supersaturation and chemical composition of the system. The analysis of the composition of the droplet shows that the mole fractions fluctuate throughout the nucleation process and depart from the composition of the bulk. This departure is however found to become less and less significant as the size of the droplet increases and its composition starts to conform more and more to that predicted by thermodynamics. Finally, while the $\mu_1\mu_2VT - S$ does not yield directly the nucleation rate, the method allows to generate and stabilize configurations of the system close to the top of the free energy barrier. However, as discussed in previous work¹⁹, the nucleation rate can be obtained by carrying out additional molecular molecular dynamics simulations, using configurations close to the top of the free energy barrier as a starting point, and following the Bennett-Chandler scheme^{103–105} to determine the kinetics of the process. Alternatively, the threshold method of Yasuoka and Matsumoto can also be used to determine the nucleation rate¹.

Acknowledgements Partial funding for this research was provided by NSF through CAREER award DMR-1052808.

¹ K. Yasuoka and M. Matsumoto, *J. Chem. Phys.* **109**, 8451 (1998).

² D. W. Oxtoby, *J. Phys. Condens. Matter* **4**, 7627 (1992).

³ V. K. Shen and P. G. Debenedetti, *J. Chem. Phys.* **111**, 3581 (1999).

⁴ C. L. Weakliem and H. Reiss, *J. Chem. Phys.* **99**, 5374 (1993).

- ⁵ G. K. Schenter, S. M. Kathmann, and B. C. Garrett, *Phys. Rev. Lett.* **82**, 3484 (1999).
- ⁶ X. C. Zeng and D. W. Oxtoby, *J. Chem. Phys.* **94**, 4472 (1991).
- ⁷ P. Yi, D. Poulikakos, J. Walther, and G. Yadigaroglu, *Int. J. Heat Mass Tran.* **45**, 2087 (2002).
- ⁸ T. Kinjo, K. Ohguchi, K. Yasuoka, and M. Matsumoto, *Comput. Mater. Sci.* **14**, 138 (1999).
- ⁹ S. Toxvaerd, *J. Chem. Phys.* **115**, 8913 (2001).
- ¹⁰ I. Ford, *J. Chem. Phys.* **105**, 8324 (1996).
- ¹¹ V. Talanquer and D. Oxtoby, *J. Phys. Chem.* **99**, 2865 (1995).
- ¹² H. Reiss, A. Tabazadeh, and J. Talbot, *J. Chem. Phys.* **92**, 1266 (1990).
- ¹³ V. Kalikmanov and M. Van Dongen, *J. Chem. Phys.* **103**, 4250 (1995).
- ¹⁴ M. Horsch, J. Vrabec, and H. Hasse, *Phys. Rev. E* **78**, 011603 (2008).
- ¹⁵ A. V. Neimark and A. Vishnyakov, *J. Chem. Phys.* **122**, 054707 (2005).
- ¹⁶ D. W. Oxtoby and R. Evans, *J. Chem. Phys.* **89**, 7521 (1988).
- ¹⁷ J. F. Lutsko, *J. Chem. Phys.* **129**, 244501 (2008).
- ¹⁸ Z.-J. Wang, C. Valeriani, and D. Frenkel, *J. Phys. Chem. B* **113**, 3776 (2008).
- ¹⁹ P. R. Ten Wolde, M. J. Ruiz-Montero, and D. Frenkel, *J. Chem. Phys.* **110**, 1591 (1999).
- ²⁰ M. A. Gonzalez, J. L. Abascal, C. Valeriani, and F. Bresme, *J. Chem. Phys.* **142**, 154903 (2015).
- ²¹ T. D. Loeffler, A. Sepehri, and B. Chen, *J. Chem. Theory Comput.* **11**, 4023 (2015).
- ²² G. C. Sosso, J. Chen, S. J. Cox, M. Fitzner, P. Pedevilla, A. Zen, and A. Michaelides, *Chem. Rev.* (2016).
- ²³ W. Xu, Z. Lan, B. Peng, R. Wen, and X. Ma, *J. Chem. Phys.* **142**, 054701 (2015).
- ²⁴ S. J. Keasler and J. I. Siepmann, *J. Chem. Phys.* **143**, 164516 (2015).
- ²⁵ Ø. Wilhelmsen, T. T. Trinh, S. Kjelstrup, and D. Bedeaux, *J. Phys. Chem. C* **119**, 8160 (2015).
- ²⁶ J. van Meel, Y. Liu, and D. Frenkel, *Mol. Phys.* **113**, 2742 (2015).
- ²⁷ B. N. Hale, *Phys. Rev. A* **33**, 4156 (1986).
- ²⁸ B. N. Hale, *J. Chem. Phys.* **122**, 204509 (2005).
- ²⁹ B. N. Hale and M. Thomason, *Phys. Rev. Lett.* **105**, 046101 (2010).
- ³⁰ D. Yuhara, B. C. Barnes, D. Suh, B. C. Knott, G. T. Beckham, K. Yasuoka, D. T. Wu, and A. K. Sum, *Faraday Discuss.* **179**, 463 (2015).
- ³¹ M. Lauricella, S. Meloni, S. Liang, N. J. English, P. G. Kusalik, and G. Ciccotti, *J. Chem. Phys.* **142**, 244503 (2015).

- ³² J. K. Singh and F. Müller-Plathe, *Appl. Phys. Lett.* **104**, 021603 (2014).
- ³³ R. Ni and M. Dijkstra, *Soft Matter* **9**, 365 (2013).
- ³⁴ A. Reinhardt and J. P. Doye, *J. Chem. Phys.* **141**, 084501 (2014).
- ³⁵ P. R. Ten Wolde and D. Frenkel, *J. Chem. Phys.* **109**, 9901 (1998).
- ³⁶ B. Chen, J. I. Siepmann, K. J. Oh, and M. L. Klein, *J. Chem. Phys.* **115**, 10903 (2001).
- ³⁷ K. Oh and X. C. Zeng, *J. Chem. Phys.* **110**, 4471 (1999).
- ³⁸ B. Chen, J. I. Siepmann, K. J. Oh, and M. L. Klein, *J. Chem. Phys.* **116**, 4317 (2002).
- ³⁹ D. Zhukhovitskii, *J. Chem. Phys.* **103**, 9401 (1995).
- ⁴⁰ K. Nishi, S. Inoue, and Y. Matsumura, *Chem. Phys. Lett.* **634**, 194 (2015).
- ⁴¹ L. Lupi, B. Peters, and V. Molinero, *J. Chem. Phys.* **145**, 211910 (2016).
- ⁴² E. E. Santiso and B. L. Trout, *J. Chem. Phys.* **143**, 174109 (2015).
- ⁴³ J. T. Berryman, M. Anwar, S. Dorosz, and T. Schilling, *J. Chem. Phys.* **145**, 211901 (2016).
- ⁴⁴ N. E. Zimmermann, B. Vorselaars, D. Quigley, and B. Peters, *J. Am. Chem. Soc.* **137**, 13352 (2015).
- ⁴⁵ J. Lam, D. Amans, C. Dujardin, G. Ledoux, and A.-R. Allouche, *J. Phys. Chem. A* **119**, 8944 (2015).
- ⁴⁶ K. Kratzer and A. Arnold, *Soft matter* **11**, 2174 (2015).
- ⁴⁷ P. Bolhuis and C. Dellago, *Eur. Phys. J. Special Topics* **224**, 2409 (2015).
- ⁴⁸ G. V. Lau, P. A. Hunt, E. A. Müller, G. Jackson, and I. J. Ford, *J. Chem. Phys.* **143**, 244709 (2015).
- ⁴⁹ S. Toxvaerd, *J. Chem. Phys.* **144**, 164502 (2016).
- ⁵⁰ K. K. Tanaka, K. Kawamura, H. Tanaka, and K. Nakazawa, *J. Chem. Phys.* **122**, 184514 (2005).
- ⁵¹ T. Kraska, *J. Chem. Phys.* **124**, 054507 (2006).
- ⁵² K. Oh and X. C. Zeng, *J. Chem. Phys.* **112**, 294 (2000).
- ⁵³ B. Senger, P. Schaaf, D. Corti, R. Bowles, D. Pointu, J.-C. Voegel, and H. Reiss, *J. Chem. Phys.* **110**, 6438 (1999).
- ⁵⁴ M. Kulmala and A. Laaksonen, *J. Chem. Phys.* **93**, 696 (1990).
- ⁵⁵ X. C. Zeng and D. Oxtoby, *J. Chem. Phys.* **95**, 5940 (1991).
- ⁵⁶ D. W. Oxtoby and D. Kashchiev, *J. Chem. Phys.* **100**, 7665 (1994).
- ⁵⁷ I. Napari and A. Laaksonen, *J. Chem. Phys.* **111**, 5485 (1999).

- ⁵⁸ A. Jaecker-Voirol and P. Mirabel, *J. Phys. Chem.* **92**, 3518 (1988).
- ⁵⁹ V. Talanquer and D. W. Oxtoby, *J. Chem. Phys.* **102**, 2156 (1995).
- ⁶⁰ P. R. ten Wolde and D. Frenkel, *J. Chem. Phys.* **109**, 9919 (1998).
- ⁶¹ A. Laaksonen and D. W. Oxtoby, *J. Chem. Phys.* **102**, 5803 (1995).
- ⁶² S. Yoo, K. Oh, and X. C. Zeng, *J. Chem. Phys.* **115**, 8518 (2001).
- ⁶³ I. Napari and A. Laaksonen, *Phys. Rev. Lett.* **84**, 2184 (2000).
- ⁶⁴ S. Braun, V. Kalikmanov, and T. Kraska, *J. Chem. Phys.* **140**, 124305 (2014).
- ⁶⁵ R. Shimizu and H. Tanaka, *Nature Commun.* **6**, 7407 (2015).
- ⁶⁶ B. Pinho, S. Girardon, F. Bazer-Bachi, G. Bergeot, S. Marre, and C. Aymonier, *Lab on a Chip* **14**, 3843 (2014).
- ⁶⁷ X. Gao, D. Fu, B. Xie, Y. Su, and D. Wang, *J. Phys. Chem. B* **118**, 12549 (2014).
- ⁶⁸ N. V. Alekseechkin, *J. Chem. Phys.* **143**, 054502 (2015).
- ⁶⁹ K. D. Watson, S. T. Nguelo, C. Desgranges, and J. Delhommelle, *CrystEngComm* **13**, 1132 (2011).
- ⁷⁰ C. Desgranges and J. Delhommelle, *J. Am. Chem. Soc.* **136**, 8145 (2014).
- ⁷¹ C. Desgranges and J. Delhommelle, *J. Chem. Phys. - Part I* (accepted for publication) (2016).
- ⁷² R. McGraw and A. Laaksonen, *Phys. Rev. Lett.* **76**, 2754 (1996).
- ⁷³ G. M. Torrie and J. P. Valleau, *J. Comput. Phys.* **23**, 187 (1977).
- ⁷⁴ M. P. Allen and D. J. Tildesley, *Computer Simulation of Liquids* (Clarendon Press, Oxford, 1987).
- ⁷⁵ C. Desgranges and J. Delhommelle, *J. Phys. Chem. C* **113**, 3607 (2009).
- ⁷⁶ C. Desgranges and J. Delhommelle, *J. Chem. Phys.* **127**, 144509 (2007).
- ⁷⁷ J. Vrabec, J. Stoll, and H. Hasse, *J. Phys. Chem. B* **105**, 12126 (2001).
- ⁷⁸ J. J. Potoff, J. R. Errington, and A. Z. Panagiotopoulos, *Mol. Phys.* **97**, 1073 (1999).
- ⁷⁹ J. R. Errington and A. Z. Panagiotopoulos, *J. Phys. Chem. B* **103**, 6314 (1999).
- ⁸⁰ J. R. Errington and A. Z. Panagiotopoulos, *J. Chem. Phys.* **111**, 9731 (1999).
- ⁸¹ J. R. Errington, *J. Chem. Phys.* **118**, 9915 (2003).
- ⁸² C. Desgranges and J. Delhommelle, *J. Chem. Phys.* **140**, 104109 (2014).
- ⁸³ C. Desgranges and J. Delhommelle, *J. Chem. Phys.* **136**, 184107 (2012).
- ⁸⁴ C. Desgranges and J. Delhommelle, *J. Chem. Phys.* **136**, 184108 (2012).
- ⁸⁵ C. Desgranges and J. Delhommelle, *J. Chem. Phys.* **144**, 124510 (2016).

- ⁸⁶ G. Gazenmüller and P. J. Camp, *J. Chem. Phys.* **127**, 154504 (2007).
- ⁸⁷ Y. Liu, A. Z. Panagiotopoulos, and P. G. Debenedetti, *J. Phys. Chem. B* **115**, 6629 (2011).
- ⁸⁸ I. Nezbeda and J. Kolafa, *Molec. Simul.* **5**, 391 (1991).
- ⁸⁹ J. K. Singh and J. R. Errington, *J. Phys. Chem. B* **110**, 1369 (2006).
- ⁹⁰ N. Rai, J. I. Siepmann, N. E. Schultz, and R. B. Ross, *J. Phys. Chem. C* **111**, 15634 (2007).
- ⁹¹ K. S. Rane, S. Murali, and J. R. Errington, *J. Chem. Theory Comput.* **9**, 2552 (2013).
- ⁹² F. Escobedo and J. J. de Pablo, *J. Chem. Phys.* **105**, 4391 (1996).
- ⁹³ W. Shi and E. J. Maginn, *J. Comp. Chem.* **29**, 2520 (2008).
- ⁹⁴ H. Eslami and F. Müller-Plathe, *J. Comput. Chem.* **28**, 1763 (2007).
- ⁹⁵ P. S. Vogt, R. Liapine, B. Kirchner, A. J. Dyson, H. Huber, G. Marcelli, and R. J. Sadus, *Phys. Chem. Chem. Phys.* **3**, 1297 (2001).
- ⁹⁶ B. Widom, *J. Chem. Phys.* **39**, 2808 (1963).
- ⁹⁷ J. Siepmann and D. Frenkel, *Mol. Phys.* **75**, 59 (1992).
- ⁹⁸ H. Reiss, *J. Chem. Phys.* **18**, 840 (1950).
- ⁹⁹ B. Wyslouzil and J. Seinfeld, *J. Chem. Phys.* **97**, 2661 (1992).
- ¹⁰⁰ J. Wedekind, D. Reguera, and R. Strey, *J. Chem. Phys.* **127**, 064501 (2007).
- ¹⁰¹ G. Wilemski, *Journal of Physical Chemistry* **91**, 2492 (1987).
- ¹⁰² I. Napari, A. Laaksonen, V. Talanquer, and D. W. Oxtoby, *The Journal of chemical physics* **110**, 5906 (1999).
- ¹⁰³ C. H. Bennett, *Algorithms for chemical computations* (ACS symposium Series, vol. 46, American Chemical Society, Washington DC, 1977).
- ¹⁰⁴ D. Chandler, *J. Chem. Phys.* **68**, 2959 (1978).
- ¹⁰⁵ E. Carter, G. Ciccotti, J. T. Hynes, and R. Kapral, *Chem. Phys. Lett.* **156**, 472 (1989).